WPMST1-PR(17) 17591

C K Tsui et al.

Poloidal Asymmetry in the Narrow Heat Flux Feature in the TCV Scrape-Off Layer

Preprint of Paper to be submitted for publication in
Physics of Plasmas

This work has been carried out within the framework of the EUROfusion Consortium and has received funding from the Euratom research and training programme 2014-2018 under grant agreement No 633053. The views and opinions expressed herein do not necessarily reflect those of the European Commission.

This document is intended for publication in the open literature. It is made available on the clear understanding that it may not be further circulated and extracts or references may not be published prior to publication of the original when applicable, or without the consent of the Publications Officer, EUROfusion Programme Management Unit, Culham Science Centre, Abingdon, Oxon, OX14 3DB, UK or e-mail Publications.Officer@euro-fusion.org

Enquiries about Copyright and reproduction should be addressed to the Publications Officer, EUROfusion Programme Management Unit, Culham Science Centre, Abingdon, Oxon, OX14 3DB, UK or e-mail Publications.Officer@euro-fusion.org

The contents of this preprint and all other EUROfusion Preprints, Reports and Conference Papers are available to view online free at http://www.euro-fusionscipub.org. This site has full search facilities and e-mail alert options. In the JET specific papers the diagrams contained within the PDFs on this site are hyperlinked

Poloidal Asymmetry in the Narrow Heat Flux Feature in the TCV Scrape-Off Layer

C.K. Tsui[1,2], J.A. Boedo[1], F.D. Halpern[3], J. Loizu[4], F. Nespoli[2], J. Horacek[5], B. Labit[2], J. Morales[2], H. Reimerdes[2], P. Ricci[2], C. Theiler[2], S. Coda[2], I. Furno[2], The TCV Team[2] and the EUROfusion MST1 Team[*]

[1]University of California-San Diego, La Jolla, California 92093, USA
[2]Swiss Plasma Center (SPC), Ecole Polytechnique Federale de Lausanne (EPFL), CH-1015 Lausanne, Switzerland
[3]General Atomics, P.O. Box 85608, San Diego, California 92186-9784
[4]Max-Planck-Institut für Plasmaphysik, D-17491 Greifswald, Germany
[5]IPP.CR, Institute of Plasma Physics AS CR, Za Slovankou 3, 182 21 Praha 8, Czech Republic
Corresponding Author: C7Tsui@ucsd.edu

Abstract

Heat flux profiles inferred from a reciprocating probe at the outer midplane of the TCV tokamak during inner wall limited discharges feature radial fall-off lengths that shorten near the last closed flux surface (LCFS) consistent with the so-called "narrow feature". The narrow feature is significantly wider on the outboard side compared with that measured on the inner wall by infrared (IR) thermography, so it is difficult to discern from the main SOL feature. After small shifts were applied for alignment, the fraction of the power contained in the narrow feature matches between inboard and outboard measurements and they scale together with plasma current I_p, suggesting that we are observing the same phenomenon.

The outboard side fall-off length within the narrow feature is found to scale closely with the radial correlation length of the edge turbulence as expected if the narrow feature arises due to radially sheared ExB flows. This is found to hold true even for cases where the narrow feature is weak and the fall-off lengths are approaching that of the far scrape-off layer.

After the small shifts for alignment, non-zero floating potential profiles were found to match between inboard and outboard sides. A simple model of polarization and diamagnetic cross-field currents is described, which is consistent with the shape of these floating potential profiles. The model predicts that the floating potential at the LCFS must be negative, which supports the argument to shift the upstream measurements. The predicted currents are also consistent with the ExB flows believed to cause the narrow feature. The model is used to predict the magnitude of the floating potential of the LCFS, and the results are found to match measurements for all values of I_p.

This paper therefore demonstrates consistency between the measurements of the narrow feature on the inboard and outboard sides of the plasma, as well as consistency between the measurements, non-linear turbulence simulations, and analytical models of the narrow feature arising from sheared ExB flows.

[*] See the author list of H. Meyer et al., Nuclear Fusion FEC 2016 Special Issue (2017)

1. Introduction

ITER will ramp-up with an inner wall limited (IWL) plasma, with parallel heat fluxes of about 25 MW/m^2 to the central column for more than 10 s before divertor formation becomes possible [1,2]. The ITER central column first wall modules were designed to distribute heat fluxes assumed to be described by a single exponential fall-off length of a few cm [1,3]. This decision was based on a multi-machine database of heat flux profiles for IWL plasmas using reciprocating probe measurements from the outboard side scrape-off layer (SOL), [4–7] which were found to be approximately exponential.

However, heat flux profiles taken on the inboard side using infrared (IR) thermography show that the heat flux is several times higher than predicted in a narrow region just outside the last closed flux surface (LCFS). This narrow feature was first observed in limiter machines in the 1980s and 90s [8–11], but the importance of this phenomenon was not realized until dedicated experiments were performed in JET [12] with follow-up experiments in other machines [13–15], including one experiment at DIII-D where IR measurements and an inboard side swinging reciprocating probe [16] found matching results [17]. The narrow feature has been shown to increase the peak parallel heat flux by factors of 2-7 [18], exceeding engineering tolerances. Indeed, melting at the apex of JET's ITER-like central column limiters [19,20] is now believed to have been caused by the narrow feature [21].

Following the discovery of the narrow feature, additional outboard side measurements were taken in dedicated experiments with no consensus being reached whether the narrow feature existed on the outboard side. Alcator C-Mod RCP measurements show narrow features match in multiple poloidal locations in IWL plasmas [15], and diverted plasmas as well [22], which has not been reported in other machines. Experiments in COMPASS [13] found a modest change in fall-off length of the outboard RCP heat flux profiles, but this was found to always be at or inside the LCFS. DIII-D experiments found little clear indication of the narrow

feature from the outboard side or the bottom of the plasma [17]. A recent study in KSTAR reported that the narrow feature was observed on the outboard side, roughly matching the IR camera results on the inboard side [23]. Within these references, the discussion of outboard side measurements of the narrow feature is limited, further suggesting that no clear conclusions have been made.

It was necessary to redesign the ITER central column to accommodate for the narrow feature before a physics understanding of the phenomenon could be developed [18]. These insights are badly needed, or future fusion devices will continue to be vulnerable to unpredicted heat fluxes.

In this paper, we will attempt to unify the existing multi-machine dataset by explaining why the narrow feature is nearly ubiquitous in inboard side measurements while it is rarely observed in outboard side measurements [13–15,17]. We will examine in detail how the LCFS is identified in upstream measurements in sections 2.2 and 2.3 since this determination strongly influences the identification of the narrow feature. In section 2.4, we will show that the narrow feature does exist on the outboard side, but that it is easy to overlook because it is weaker in $q_{\parallel}$ magnitude and has a longer fall-off length compared to the inboard side. In section 3.1, we will show that the narrow features on the inboard side and outboard side contain a constant fraction of the SOL power, and that this fraction varies with plasma current I_p. The fall-off length of the narrow feature also varies with I_p consistent with predictions of turbulence-based models describing the narrow feature. In section 3.2, we investigate the differences between the inboard and outboard side measurements, and show that the poloidal asymmetries are similar to those seen in numerical simulations. Finally, in section 3.3 we will test predictions of turbulence-based models describing the narrow feature in relation to cross-field current circulation in the SOL.

2. Experimental Methods

The experiments were performed in the Tokamak à Configuration Variable (TCV) which has central column tiles that were shaped in order to minimize the heat fluxes [24]. Previous work [25,26] describes the set of inner wall limited discharges,

in which scans of plasma current I_p, line average density $\langle n_e \rangle$, elongation κ, and triangularity δ were performed in deuterium and helium. These studies confirmed the existence of a sharp narrow feature a few mm wide on the inboard side based on the IR camera measurements. The wall Langmuir probes were used to show that currents flow towards the target in the first few mm, resulting in a negative drop in floating potential V_f. It was also shown that the amplitudes of the V_f drop and the narrow feature were correlated and that both decrease in magnitude with increasing collisionality. At high collisionality (exact values depend on how it's calculated [25,26]) the $q_{\parallel}$ profile could be described by a single fall-off length λ_q for the entire SOL, and V_f =0V across the entire SOL.

In this work, we limited our discussion to results from the I_p scan in deuterium with major radius R = 0.88 m, minor radius a = 0.22 m, κ = 1.4, δ = 0, $\langle n_e \rangle$ =2.4X10^{19} ± 0.3X10^{19} m^{-3}. A characteristic equilibrium is shown in Figure 1 with the locations of the reciprocating probe, the IR camera field of view, and the wall Langmuir Probes[27] labeled therein. The Last Closed Flux Surface (LCFS) obtained from LIUQE equilibrium reconstruction is shown by the thick line, which is limited against the inboard wall on the left. I_p was scanned from discharge to discharge from a minimum of 85 kA to a maximum of 210 kA (see Figure 2 a). The line averaged density (b) was held constant across the scan, and was stable from 0.4s through to the end of the discharges. The ohmic power varies with I_p, and is also well controlled. RCP data was taken at 1.6 s, which is during the steady-state phase of the discharge.

2.1. The fast reciprocating probe

The outboard side measurements were taken using a 10 electrode fast reciprocating probe [28], which is actuated using a helium piston driven at 60 psi. A linear potentiometer is used to record the reciprocation depth as a function of time, which is then used to determine the electrode position within the plasma vessel. The probe moves relatively slowly when compared to plasma control system timescales (see Figure 3). Therefore, the normalized coordinates ($R - R_{sep}$ taken at the outer mid-

plane) shown in this paper have been calculated at 1ms time resolution, which corrects for these oscillations in the LCFS position. The electrodes are arranged as several individual diagnostics (see Figure 4). The double probe consists of two electrodes, and the power supplies that provide a bias between them. The entire system is electrically isolated and maintains a voltage at the floating potential of the plasma, reducing the power supply requirements needed to maintain saturation. The voltage across the two electrodes is swept ±300 V at 1kHz, providing I-V characteristics every 0.5 ms with fitted values of electron temperature T_e, saturation current J_{sat} and electron density n_e. For this study, we utilized a sheath expansion corrected I-V fitting function which is described in more detail in [29]:

$$I = J_{sat} \bullet A_{coll} \bullet \tanh\left(\frac{V - V_{off}}{2kT_e / e}\right) + I_{off} \qquad \textbf{Eqn 1a}$$

$$A_{coll} = A_0 + l_p l_{sh} \qquad \textbf{Eqn 1b}$$

$$l_{sh} = \lambda_{Debye}\left|\frac{V - V_p}{kT_e / e}\right|^{3/4} \qquad \textbf{Eqn 1c}$$

I_{off}, and V_{off} are fitted parameters that exist only to ensure the tanh function is fit to symmetric data. The collection area A_{coll} accounts for sheath expansion using the Child-Langmuir law (Eqn 1c). A_0 is the surface area of the electrode, l_p is the effective perimeter of the electrode, which is approximated as $l_p = 3\sqrt{A_0}$, l_{sh} is the Debye sheath thickness, and λ_{Debye} is the Debye length.

The fluctuations diagnostic is comprised of an ion saturation electrode (biased to -400V) and an array of 5 floating potential electrodes, designed for a bandwidth ranging from dc to 5 MHz. In these ohmic discharges, the spectral power of the I_{sat} and V_f signals drop to the noise floor at approximately 300kHz.

2.2. Identifying the last closed flux surface

In order to assess the existence of the narrow feature, it is essential to know the location of the LCFS with an uncertainty that is of similar or smaller width to the radial fall-off length of this feature. We will show that the profile alignment uncertainty between the measurements from the RCP and those taken at the central

column can be reduced to the radial length of the electrodes for sheath-limited conditions.

In the TCV tokamak, the plasma equilibrium is calculated using the LIUQE code [30]. The noise in the magnetic probes signals, and spatial alignment errors accumulate in the equilibrium reconstruction resulting in a systematic error in the radius of the LCFS that is typically less than ± 5mm (see section 2.3), so it is commonly necessary to apply small shifts to correct profile coordinates.

The LCFS position can be estimated via power balance [31,32], but a significant power balance shortfall is observed in TCV with the output power determined from either the RCP $q_{\parallel}$, the IR camera $q_{\parallel}$, or even the IR camera $q_{\perp}$ (which should double-count some portion of the radiated power). This is due in part to the fact that the bolometric system in TCV underestimates the radiated power because the gold foil bolometers are reflective at visible wavelengths, and thus underestimate the radiated power by a minimum of 13-15% [33].

In the simplest case of no sheath currents, the floating potential of a Langmuir probe is $V_f \cong 0$ V throughout the SOL until the probe crosses the LCFS at which point V_f begins to drop sharply as the radial electric field E_r is determined by the force balance equation [34]. The transition makes the RCP a self-aligning diagnostic, allowing us to identify the location of the LCFS with an accuracy of ± 2-5 mm depending on plasma conditions and interpretation methodology. However, this approach provides a marginal improvement in precision with respect to the LCFS obtained from equilibrium reconstruction, and therefore it is still not accurate enough to allow a clear identification of the narrow feature.

Figure 5 shows V_f as measured by the flush-mounted wall probes and the RCP taken in the same discharges for three values of I_p with corresponding SOL collisionality values ν^*_{SOL} [35] calculated from upstream plasma conditions taken from the RCP near the LCFS. The profiles are shifted to overlap. The wall-mounted probes show a drop in V_f within the SOL which have been shown to increase in magnitude with decreasing collisionality [25,26]. The fact that the V_f drop extends a short distance into the SOL is an important prediction for a turbulence model and

simulation describing the narrow feature [36] which will be discussed in section 3. V_f is also seen to form a positive non-zero feature spanning from $R - R_{sep}$ = 2mm to 10mm into the SOL which balances the negative V_f drop (i.e. the total positive and negative currents to the limiter sum approximately to zero when estimated using RCP data). We will show in section 3.3 that the positive and negative features are the result of cross-field current circulation in the SOL.

In Figure 5a) where I_p =190 kA, one notes the agreement in the shape and magnitude of the sharp drop as well as in the positive feature. Similar agreement is seen for other discharges for I_p ≥110 kA (see Figure 5b where I_p =110 kA, where the features are reproduced, although a small offset is observed in the far-SOL where the collisionality is higher). Both traces become flatter with decreasing I_p with no noteworthy features (positive or negative) when I_p <100 kA as is shown in Figure 5c) with I_p =85 kA.

We assume therefore that the floating potential is approximately constant no matter where it is measured along the field-lines when the collisionality is sufficiently low (specifically, when I_p ≥110 kA, $\nu^*_{SOL} \leq 10$). We assert that shifting the RCP measurements to obtain agreement with V_f measured by the wall probes reduces the systematic error in the normalized coordinates between these two locations down to the radial length of the electrodes (± 0.75 mm). The profiles in this paper have therefore been shifted by a few mm (from the LIUQE estimate –solid blue line- to the current axis –dashed line- in Figure 5) to align the V_f profiles between upstream and target measurements.

For cases where I_p <100 kA, aligning the profiles is more difficult, and the RCP profile is shifted such that the drop in V_f is placed just inside the LCFS, such that V_f is approximately constant outside the LCFS in agreement with the wall probes. We note however, that radial fall-off lengths are large and relatively constant for these cases, and that the narrow feature is negligibly small regardless of any shifts made to the RCP profiles.

Furthermore, for conditions where collisionality is low (i.e. the I_p =190 kA ν^*_{SOL} =2.5 case) the absolute uncertainty in the location of the LCFS in the RCP profiles has

also been reduced such that it is comparable to the uncertainty of the LCFS location from the wall probe measurements, which is mainly due to tile misalignment and to the error in the height of the magnetic axis in the LIUQE reconstruction. Requiring that $V_f < 0$ at the LCFS is consistent with an analytical model that the narrow feature arises from sheared ExB flows [36], non-linear turbulence simulations of the narrow feature [36], the SOL-current model (section 3.3), as well as SOL current balance against the $V_f > 0$ feature. We estimate the total uncertainty in the LCFS position to be (-1.5mm, +0.75mm) for the lowest collisionality discharges. Having this level of accuracy in the location of the LCFS provides an opportunity to evaluate other commonly used methods for defining the location of the LCFS in upstream measurements.

2.3. Alternative methods for identifying the last closed flux surface

In order to compare profile measurements at different poloidal locations, it is standard practice to apply small shifts to the profiles to correct for errors in the magnetic reconstruction. While there is no standard practice in the field, the data in this study suggest that the narrow feature and its associated SOL-currents have a confounding effect on two methods that are commonly used with reciprocating probes. It is therefore important to understand how the accuracy of these methods change in conditions where the narrow feature is present.

1.1.1. The maximum gradient in E_r

The first method we shall evaluate is that the LCFS coincides with the maximum gradient in E_r, or at the minimum in the second derivative of the plasma potential $\partial^2 V_{pl} / \partial R^2$. This prescription is supported by work in stellarators [37] where the LCFS position can be verified when no plasma is present. However, this method has its drawbacks. The uncertainty is typically large when taking the second derivative of a measured quantity, and the result depends strongly on how the data is fit or smoothed. Furthermore, it is difficult to measure V_p directly, so it is typically necessary to calculate it as $V_p = V_f + 2.5T_e$, necessitating a fit of the T_e profile as well,

and introducing the scatter in that quantity. Example fits of V_p and V_f are shown in Figure 6 (a) and their second derivatives are shown in Figure 6 (b) for the I_p = 190 kA case. 9th order polynomials fits were used for V_f and T_e to provide close fits with dynamic 2nd derivatives. This results in some over-fitting where the profiles truncate, but not in the region of interest. The grey region in (a) shows the scatter in the V_f measurement from intermittency. The grey line in (b) shows $\partial^2 V_f / \partial R^2$ taken from local 2nd order polynomials fit over 5mm of data, and is meant to represent the scatter in that value. The scatter in V_p and $\partial^2 V_{pl} / \partial R^2$ are not shown, as they are off-scale. The minima in the polynomial fits to $\partial^2 V_f / \partial R^2$ and $\partial^2 V_{pl} / \partial R^2$ agree, likely because the fits tend to smooth. It is possible that higher resolution T_e profiles would produce a sharper inflection point, affecting the minimum more.

We find that the minimum in $\partial^2 V_f / \partial R^2$ occurs 1-3mm outside the LCFS, roughly where V_f =0, and therefore violating SOL current balance. The SOL-currents associated with the narrow-feature require that V_f drops quickly in a region outside the LCFS roughly the width of the poloidal gyro radius (~7mm in this case). This pushes the minimum in $\partial^2 V_f / \partial R^2$ away from the LCFS and into the SOL.

1.1.2. The velocity shear layer

The second method we will evaluate proposes that the poloidal phase velocity of the turbulent structures have opposite signs on either side the 'Velocity Shear Layer' (VSL), and that the VSL coincides with the LCFS [38]. This method is attractive because the change in sign of the poloidal phase velocity occurs rather abruptly, and its location tends to be invariable with differences in methodology in calculating the phase velocity.

To find the VSL location, we used the cross-correlation method [38–40] between the floating potential from two poloidally separated V_f electrodes. A bandpass filter was first applied to the V_f traces with a low cutoff frequency of 12 kHz, which is just above the 10 kHz typical switching frequency of the fast power supply that drives TCV's vertical stability control coils[41]. The high cut-off frequency has little effect

on the cross-correlation results so long as it is set above the noise floor at 300kHz, so for this paper it was set at 1.2 MHz, which is just below the Nyquist frequency. The cross-correlation was applied over 250 μs time windows as:

$$\left(V_{f-1} \bigstar V_{f-2}\right)(\tau) = \int_{t_0-125\mu s}^{t_0+125\mu s} V_{f-1}(t) V_{f-2}(t+\tau)\, dt \qquad \textbf{Eqn 2}$$

This time window typically contains between 5-9 distinct turbulence events. A Gaussian was fit to the resulting function which has a width defined as the decorrelation time τ_c and which is centered at τ_{shift}, representing the average time delay between the passing of a turbulent structure over the two separated electrodes. The poloidal velocity is calculated as

$$V_{\perp} = \delta_z / \tau_{shift} \qquad \textbf{Eqn 3}$$

where δ_z is the vertical separation between the electrodes. See example in Figure 6 c). The square datapoints were calculated using the $V_{f\text{-}mid}$ and $V_{f\text{-}top}$ electrodes (electrodes are labeled in Figure 4), which are separated by δ_z = 4mm. The triangle datapoints were calculated using the $V_{f\text{-}bottom}$ and $V_{f\text{-}top}$ electrodes, which are separated by δ_z = 10mm. The two datasets agree well, and both show an abrupt change in sign 3.8 mm outside the LCFS. The actual change in phase velocity has been shown to occur more gradually when the radial phase velocity is accounted for [38], but this does not change the radius at which the phase velocity changes sign, so it does not change the predicted radius for the LCFS.

The VSL occurs close to the maximum in V_p, which is consistent with the theory that one of the main driving forces for the poloidal velocity is $\left(E_r \times B_\phi\right) / B_\phi^2$. The VSL systematically occurs outside of the LCFS. If (as we believe) the narrow feature is caused by a region of poloidal velocity shear that exists just outside the LCFS (see section 3 and [36]), then it is likely that the VSL should also be pushed into the SOL by a distance on the order of the width of the narrow feature.

In Figure 5, the vertical lines represent different methods used to identify the location of the LCFS in RCP profiles. The black dashed line is at R-Rsep = 0 and is the LCFS location defined by enforcing agreement in V_f. The solid dark blue line indicates the normalized coordinate of the LCFS defined by the LIUQE equilibrium

reconstruction code. The dotted purple line represents the minimum in $\partial^2 V_f / \partial R^2$, and the dot-dashed red line represents the VSL.

As expected, these methods for defining the LCFS disagree by several mm. LIUQE appears to have a random uncertainty, disagreeing with our prescription by up to 4 mm. As the narrow feature diminishes, the disagreement between these methods becomes smaller (Figure 5 b). Then, at the highest collisionality (Figure 5 c), the change in the V_f gradient has become more subtle, and the poloidal phase velocities are small. The weaker transition increases the uncertainties for all alignment methods (except for LIUQE) making the disagreement become correspondingly larger.

It is important to note that the VSL and the minimum in $\partial^2 V_f / \partial R^2$ occur due to the transition from closed to open field-lines, and that both phenomenon occur close to the LCFS. Their precision is well within the poloidal gyro radius for all conditions tested (ρ_{pol} =7 mm for I_p = 190 kA). That is to say that the VSL and the min $\partial^2 V_f / \partial R^2$ methods are not incorrect, but their accuracy is limited to several Larmor radii. Specifically, the accuracy in locating the LCFS is wider than the precision with which one can identify the VSL or the minimum in $\partial^2 V_f / \partial R^2$. Caution is advised for any study which depends on an alignment accuracy better than several Larmor radii (which includes this paper).

2.4. Determining $q_{||}$ from reciprocating probe measurements

We estimate the parallel heatflux using the sheath-limited approximation, and normalize all values and coordinates to the outer mid plane (OMP) consistent with [12,25,26].

$$q_{||} = \left(\frac{B_{OMP}}{B_{t\arg}} \right) \left(\gamma j_{sat} \frac{kT_e}{e} + j_{sat} \varepsilon_{pot} \right) \qquad \textbf{Eqn 4}$$

We expect $\gamma = 5 \pm 3$ for fieldlines intersecting the target at angles > 1° [42], which they do for all data shown in this paper. The ε_{pot} term was set at 15.8 eV, which represents the recombination energy for D_2, and is typically negligible for these conditions. The IR camera analysis methods are discussed in [25].

Figure 7 shows T_e, and J_{sat} measured by the RCP, and the resulting $q_{||}$ for the I_p = 190 kA and I_p = 110 kA cases in the left and right columns respectively. In part c), one can clearly see that the $q_{||}$ fall off length is not constant as a function of radius, and that the profile steepens in the final 1-2 centimeter outside the LCFS and into the confined region.

The green datapoints in c) were calculated from the green T_e trendline, and the J_{sat} datapoints. These data were fitted with a sum of exponentials:

$$q_{||} = \underbrace{q_{||0}^{near} \exp\left(\frac{-\left(R - R_{sep}\right)}{\lambda_{q||}^{near}}\right)}_{\text{narrow feature}} + \underbrace{q_{||0}^{far} \exp\left(\frac{-\left(R - R_{sep}\right)}{\lambda_{q||}^{far}}\right)}_{\text{main-SOL feature}} \qquad \textbf{Eqn 5}$$

giving the fit values $\lambda_{q_{||}}^{near} = 5.1 \pm 0.5$ mm and $\lambda_{q_{||}}^{far} = 38 \pm 18$ mm. Using the blue $q_{||}$ datapoints (which are calculated using the individual T_e datapoints) produces similar results but with larger parametric uncertainties, which are given as the 2σ uncertainty calculated from the covariance matrices of the least-squares fits. The purple dot-dashed and red dashed lines represent the individual exponentials for the near-SOL and far-SOL respectively. In part h) we see a similar inflection point in the $q_{||}$ profile that occurs significantly closer to the LCFS ($\lambda_{q_{||}}^{near} = 3.4 \pm 1.2$ mm and $\lambda_{q_{||}}^{far} = 28 \pm 8$ mm). This is the lowest plasma current for which a narrow feature is discernable for the RCP data.

In parts d) and i) we compare the $q_{||}$ profile from the RCP (blue circles) against that from the IR camera (red squares). Note that the near-SOL decay length computed from the IR camera data is far smaller than that seen in the RCP data, ($\lambda_{q_{||}\,\mathrm{IR}}^{near}$ ~ 2mm for both subplots) while the $q_{||}$ decay lengths in the far-SOL nearly match. There is sufficient systematic uncertainty in the calculation of the RCP $q_{||}$ values that we cannot draw conclusions from the absolute values.

Unlike the sudden transition on the inboard side, the RCP data shows a gradual transition from a longer decay length in the far-SOL to a shorter decay length in the near-SOL that continues into the confined plasma. This is illustrated in parts e) and j) which show the local decay lengths taken from single exponential fits

centered over 2cm of the unsmoothed $q_{||}$ RCP data (grey diamonds). The local decay lengths fit over 5mm windows (blue dots) show similar trends but with more scatter (some datapoints off scale).

3. Discussion

3.1. Narrow feature I_p scalings

For comparisons against the theoretical fall-off lengths of the narrow feature, we will use $\lambda_{q||}^{LCFS}$, which is the local fall-off length taken from a single exponential fitted to the first several mm outside the LCFS. In the majority of the profiles, $\lambda_{q||}^{LCFS}$ is approximately equal to $\lambda_{q||}^{near}$ from the sum of exponential fit, but in cases where the narrow feature is weak and wide (as is the case in many of the RCP profiles), the near exponential does not represent a distinct region of the profile and $\lambda_{q||}^{near}$ becomes meaningless. This can be seen in Figure 7 h) where the purple dot-dashed line does not lay overtop of the data it is intended to represent, and the slope of the dot-dashed line is steeper than any region of the profile.

Figure 8a) shows the "narrow feature power fraction" for both the IR camera (triangles) and the RCP (diamonds) as a function of IP. We define the narrow feature power fraction as:

$$\frac{P_{near}}{P_{SOL}} \equiv \frac{P_{near}}{P_{near}+P_{far}} = \frac{q_{||0}^{near}\lambda_{q||}^{near}}{q_{||0}^{near}\lambda_{q||}^{near}+q_{||0}^{far}\lambda_{q||}^{far}} \qquad \textbf{Eqn 6}$$

There is no physical reason why P_{near}/P_{SOL} needs to agree across different poloidal locations, but it provides a way to quantify the normalized magnitude of the narrow feature that is less sensitive to minor deviations in the sum of exponentials fit than $R_q = q_{||0}^{near} \big/ q_{||0}^{far}$.

For both diagnostics, the near-SOL feature weakens with decreasing I_p and becomes vanishingly small when $I_p \leq$ 90 kA, at which point the entire SOL (both inboard and outboard) can be described by a single fall-off length equal to $\lambda_{q||}^{far}$. Good agreement is seen between the IR and RCP for P_{near}/P_{SOL} with the exception of

one outlier at I_p =210kA where P_{near} / P_{SOL} is larger for the RCP due to a larger $\lambda_{q\|}^{near}$ compared to the otherwise similar I_p =190kA discharge.

Figure 8b) shows $\lambda_{q_\|}^{LCFS}$ as a function of I_p for both diagnostics. On the outboard side, $\lambda_{q_\| \text{ RCP}}^{LCFS}$ is typically ~8mm, but as the narrow feature weakens, $\lambda_{q_\| \text{ RCP}}^{LCFS}$ grows, approaching $\lambda_{q_\|}^{far}$ = 2.5-3.5 cm. On the inboard side, $\lambda_{q_\| \text{ IR}}^{LCFS}$ follows a similar trend, but is typically ~3mm when the narrow feature is strong. A representative error bar shows the 2σ parametric uncertainty for the $\lambda_{q_\| \text{ RCP}}^{LCFS}$ series. The same error bars for $\lambda_{q_\| \text{ IR}}^{LCFS}$ are smaller than the datapoints.

For comparison, we over plotted the poloidal gyro radius, and the Larmor radius calculated at the outer LCFS as a function of B_{pol} and T_{i0} taken from the RCP data assuming $T_i = 3T_e$. This fraction is based on T_i measurements made using retarding field analyzer data in the SOL from limited plasmas [43]. $\lambda_{q_\| \text{ RCP}}^{LCFS}$ on the outboard side is on the order of the poloidal gyro radius. $\lambda_{q_\| \text{ IR}}^{LCFS}$ is significantly shorter, and on the order of the Larmor radius. The Goldston Heuristic Drift scaling is shown as it was calculated in [44,45].

$$\lambda_{q_\| \text{ Goldston}}^{LCFS} = 5671 \bullet P_{SOL}^{1/8} \frac{\left(1+\kappa^2\right)^{5/8} a^{17/8} B_t^{1/4}}{I_p^{9/8} R} \left(\frac{2\bar{A}}{1+\bar{Z}}\right)^{7/16} \left(\frac{Z_{eff}+4}{5}\right)^{1/8} \quad \text{all units SI} \qquad \textbf{Eqn 7}$$

Where P_{sol} is taken as the input power minus the radiated power, a is the minor radius, B_t is the toroidal field, R is the major radius of the magnetic axis, Z_{eff} was taken as 1.8, $\bar{A}$ was taken as 2.57, and $\bar{Z}$ was taken as 1.19. $\lambda_{q_\| \text{ Goldston}}^{LCFS}$ agrees with $\lambda_{q_\| \text{ IR}}^{LCFS}$ while the narrow feature is strong, but does not fit the data for I_p < 100kA.

A recent paper estimated the narrow feature $\lambda_{q_\|}^{LCFS}$ from a balance between perpendicular transport driven by turbulence and parallel convection [36], which is a model for transport balance in attached, sheath-limited plasmas such as the ones presented in the present work. The turbulent saturation amplitude was obtained by balancing turbulence driven radial polarization currents against large sheath flows related to a velocity shear layer. The presence of a large drop in floating potential at the LCFS, such as the ones shown in Figure 5, support the physical assumption of a

large increase of the electron parallel velocity with respect to the sound speed, which is a key assumption of the model, and agrees with GBS non-linear turbulence simulations [36]. We also confirm the presence of large fluctuations within the VSL, which was also observed in the non-linear simulations. Considering a complex interaction between non-linearly saturated turbulence, sheath flows, and ExB shear, the following closed analytical expression is given for the gradient scale length:

$$\lambda_{q_{\|}\ \text{Halpern}}^{LCFS} \approx \frac{k_x^{-1}}{2}\left(\frac{q}{\rho_*}\right)^{1/4} = \frac{L_{rad}}{2\pi}\left(\frac{q}{\rho_*}\right)^{1/4} \qquad \textbf{Eqn 8}$$

Where k_x is the radial wavenumber, q is the safety factor, taken at the LCFS, and ρ_* is the normalized Larmor radius $\equiv \rho_s / R_{mag}$ where R_{mag} is the major radius of the magnetic axis and with ρ_s taken at the outer midplane. In practice, this means that turbulent transport constrains the narrow-feature $\lambda_{q_{\|}}^{LCFS}$ to the radial correlation length of the turbulence, scaled by a factor of $(1/2\pi)(q/\rho_*)^{1/4} \sim 1$ that depends very weakly on the plasma parameters.

In order to test this model, the radial correlation length L_{rad} was calculated using the cross-correlation method shown in Eqn 2, using the same band-pass filters and time-windows. In this case, the time-traces from the two radially retracted V_f electrodes ($V_{\text{f-radial }+\phi}$ and $V_{\text{f-radial }-\phi}$ in Figure 4) were averaged together, and were cross-correlated against the signal from $V_{\text{f-mid}}$. The radial correlation length is calculated as

$$L_{rad} = \delta_r \frac{\tau_c}{\tau_{shift}} \qquad \textbf{Eqn 9}$$

where the electrodes have a radial separation of δ_r = 1.57 mm.

$\lambda_{q_{\|}\ \text{Halpern}}^{LCFS}$ was estimated by taking an average of measured L_{rad} values across the first 5 mm of the SOL. We utilized a robust mean such that values outside of 2 standard deviations were flagged as outliers and omitted from the mean. $\lambda_{q_{\|}\ \text{Halpern}}^{LCFS}$ is plotted in Figure 8b) (circles) and we note that $\lambda_{q_{\|}\ \text{Halpern}}^{LCFS}$ and $\lambda_{q\|\ \text{RCP}}^{LCFS}$ agree within the accuracy of the measurements for all values of I_p, even for conditions where the narrow feature is weak. The fact that $\lambda_{q_{\|}\ \text{Halpern}}^{LCFS}$ is approximately equal to the poloidal gyro radius is also a prediction made in [36]. However, $\lambda_{q_{\|}\ \text{Halpern}}^{LCFS}$ does not appear to

agree with the smaller values of $\lambda_{q\|\,\mathrm{IR}}^{LCFS}$, and the reason for this disagreement and for the poloidal asymmetry in general is not known. See section 3.2.

In summary, the fact that the narrow feature power fraction from the IR camera and the RCP agree and that both vanish for $I_p \leq 90$ kA suggests that the diagnostics are observing two sides of the same phenomenon. The narrow feature is expressed more prominently on the inboard side, and is wider on the outboard side. The outboard side narrow heat flux feature fall-off length $\lambda_{q\|\,\mathrm{RCP}}^{LCFS}$ matches the predicted lengths $\lambda_{q_\|\,\mathrm{Halpern}}^{LCFS}$ both for conditions where the narrow feature is strong, and (more surprisingly) for conditions where the narrow feature is weak, which lends considerable support for the model.

3.2. Poloidal Asymmetries and comparison to GBS Simulations

The poloidal asymmetry between the narrow feature observations on the inboard and outboard sides is clearly seen in Figure 7 and 8. The fact that the change in decay length presents itself rather weakly on the outboard side combined with the inherent uncertainty in the location of the LCFS explains why measurements taken in outboard and other poloidal locations in several devices [4–7, 13,17] showed little or no evidence of the narrow feature. It is thus suspected that the poloidal asymmetry in the narrow feature is inherent in the physics causing it, which can be confirmed by interrogating simulations of these IWL discharges.

Simulations using the Global Braginskii Solver (GBS) code [46] have shown a steepening in the pressure and $q_\|$ profiles which are consistent with the existence of the narrow heat flux feature [36,47]. Nespoli et al. discusses the poloidal asymmetry in depth, showing that the narrow feature occurs in the pressure channel and showing that p_0^{near} and λ_p^{near} change as a function of poloidal angle [47]. The magnitude of the narrow feature is stronger on the inboard side, and weaker on the outboard side (especially at the top of the plasma) which is consistent with our observations. λ_p^{near} changes with poloidal angle, but it increases in width, rather than decreasing in width at the target.

The theoretical analysis in [36] assumes that poloidal asymmetries are negligible, but the $q_{\|0}^{near}$ in the simulations does change by more than factor of 2. One example from the low collisionality simulation can be seen in Figure 1 in that paper (we have reproduced the relevant parts here in Figure 9a). The narrow feature on the inboard side below the limiter is clearly stronger and steeper than at the outboard midplane, while the far-SOLs are more similar in terms of fall-off length and $q_{\|}$ magnitude. The local fall-off length is shown in Figure 9b) as a function of radius for the two profiles above, showing gradual changes in fall-off length as a function of radius similar to those seen in Figure 7 e) and j).

In these simulations, the narrow feature presents itself in the macroscopic heat flux channels (i.e. the T_e and n_e profiles). The poloidal asymmetries in the narrow feature are therefore also expressed as poloidal asymmetries in the radial gradients of the T_e and n_e. This is true even in the simulations that were performed at low (i.e. sheath limited) collisionalities, where parallel temperature gradients exist due to parallel momentum loss terms that are not considered in the two point model [48]. These parallel gradients are large enough for asymmetries in the radial $q_{\|}$ gradients to exist. Indeed, this is important for the SOL current circulation model in section 3.3, which depends on poloidal asymmetry in order for the currents to close within the SOL (see the δT term in Eqn 11).

We have shown that poloidal asymmetries in the narrow feature and in the radial gradients exist in the experimental measurements and in the simulations. The simulations show an increase in the $q_{\|0}^{near}$ magnitude of the narrow feature at the target consistent with experimental measurements, but the behaviour of $\lambda_{q_{\|}}^{near}$ is not consistent. While we have demonstrated that poloidal asymmetries can and do exist, we have not found any direct reason for $q_{\|0}^{near}$ to be higher on the inboard side compared to the outboard side. The asymmetries shown in this paper suggest that the ability to predict the poloidally averaged narrow feature profile will not be sufficient, and that further study of these poloidal asymmetries is needed to be able to predict the heat flux profiles at the inner wall target.

3.3. Scrape-Off Layer Current Circulation

While sheath currents to the target are not directly responsible for the heat-flux of the narrow feature [49,50], measurements in TCV show that the amplitude of the resultant non-zero V_f at the limiter is strongly correlated with the power in the narrow feature [25,26]. Also, recent numerical simulations predict that polarization cross-field currents due to turbulent fluctuations in the near-SOL results in parallel currents flowing through the sheath [36]. The analytical model in the same reference then shows that these currents and the resulting drop in V_f are directly related to the narrow feature. We will therefore explore the physics of the circulating currents in the near-SOL with the aim of providing further insight into the narrow feature.

In addition to the contribution from the polarization cross-field current, it is further predicted [36,51] that a smaller yet opposite contribution from the diamagnetic cross-field current arises in the transition between the near-SOL and the far-SOL. Based on these facts, we use here a simple (yet useful) model that captures these effects and provides estimates for the values of V_f [51]. The model is based on an approximate time-averaged and poloidally-averaged charge balance equation, $\left\langle \nabla \bullet \mathbf{j}_{\mathbf{pol}} \right\rangle + \left\langle \nabla \bullet \mathbf{j}_{\mathbf{dia}} \right\rangle + \left\langle \nabla_{\parallel} j_{\parallel} \right\rangle = 0$, and leads to an expression for the floating potential,

$$V_f = -T_e \ln\left(1+\Delta\right) \qquad \textbf{Eqn 10}$$

where the function Δ determines whether there are electron currents to the sheath ($\Delta > 0$), no sheath currents ($\Delta = 0$), or ion currents to the sheath ($\Delta < 0$). This function is approximately given by

$$\Delta = 2\pi q \left[\frac{2}{5} \frac{1}{k_\theta \rho_s} \left(\frac{\rho_s}{\lambda_p} \right)^2 - \frac{\delta T}{T} \left(\frac{\rho_s}{\lambda_p} \right) \right] \qquad \textbf{Eqn 11}$$

where q is the safety factor, $k_\theta \rho_s \approx 0.1$ is taken to be constant, λ_p is the equilibrium pressure radial fall-off length, and $\delta T / T = \delta T_e / T_e + \delta T_i / T_i$ is the temperature poloidal asymmetry, which can be estimated with the difference between the temperatures at both ends of the field line. Here λ_p and $\delta T / T$ are seen as functions of the radius, r, and so $\Delta = \Delta(r)$. The first term in Eqn 11 is the polarization current contribution due to turbulent fluctuations and has been estimated assuming that (i) resistive ballooning modes are dominant, (ii) saturation of fluctuations occurs due to

the gradient removal mechanism [52], and (iii) there is no effect of shear flows on mode growth (which overestimates the term). The second term in Eqn 11 is the diamagnetic current contribution, which is only non-zero due to finite magnetic curvature and gradients, and whose poloidal average does not vanish when temperature asymmetries are present. Simulations have shown that $\delta T / T \sim 0.1-0.2$ [48], although these were carried out in small circular cross-sections. Finally, the parallel current has been estimated using the standard $j_{\|} = enc_s\left(1-e^{-V_f/T_e}\right)$.

The picture of how currents circulate in the SOL emerges as depicted in Figure 10. Radially increasing polarization currents push ions radially outward in the near-SOL; the sheath must then evacuate electrons to compensate the loss of charge ($V_f < 0$, region I of Figure 10). As λ_p becomes larger, the increase in polarization current is reduced; also, temperature asymmetries may have built up and produce diamagnetic currents that push electrons radially outward; the sheath is then relieved from the task of compensating ($V_f \approx 0$, $r=r_1$ in Figure 10). The polarization contribution dies out faster than the diamagnetic contribution (see Eqn 11), which leads to an effective outward push of negative charge; the sheath must now evacuate ions to compensate ($V_f > 0$, region II of Figure 10). Finally, both contributions cancel each other once again because the divergence of each current dies away ($V_f \approx 0$, $r = r_2$ in Figure 10)

Ideally, one would test this model $V_f(r)$ for all values of r, but we lack target values for T_e and any measurements of T_i within the SOL, making it difficult to estimate the diamagnetic term. It is however possible to estimate the minimum V_f value at the LCFS by considering only the polarization term. At the LCFS, we find:

$$V_{f,\min} = -T_{e0}\ln\left(1+24q\left(\frac{\rho_s}{\lambda_p}\right)^2_{\max}\right) \qquad \textbf{Eqn 12}$$

Where T_e is taken from RCP measurements, and λ_p is taken from a fit to the electron pressure profile within the narrow feature. While the scaling of this estimate is believed to be accurate, there are uncertainties of order unity in the absolute magnitude. These predictions are shown alongside the $V_{f,\min}$ measured by the wall probes as determined in [25,26] as a function of I_p in Figure 11. The model correctly predicts that the scaling of the V_f drop as a function of I_p, including the observation

that the V_f drop becomes negligible for I_p < 90 kA. This agreement suggests that this model correctly captures the physics causing the sheath currents and the sharp drop in V_f just outside the LCFS.

4. Conclusions

Measurements from a reciprocating probe on the outboard side of TCV inner wall limited plasmas were compared with IR camera and Langmuir probe measurements on inboard side with the goal of unifying the seemingly contradictory observations that the narrow feature was ubiquitously seen on the inboard side, but was rarely found on the outboard side.

Small shifts were applied to the RCP profiles to match the V_f features measured at the wall Langmuir probes for ν^*_{SOL} < 10. This LCFS position puts part of the negative drop in V_f into the SOL, as is observed at the wall probes, and disagrees with the concepts that the LCFS coincides with the minimum in $\partial^2 V_{pl} / \partial R^2$ or with the Velocity Shear Layer. This is consistent with analytical models and simulations of the narrow feature which show that the start of the drop in V_f and the region of high velocity shear is pushed into the SOL away from the LCFS by a small distance. This is also consistent with the model that the positive and negative V_f features arise due to the circulation of currents which close within the SOL.

The outboard side parallel heat fluxes were calculated using the sheath limited approximation and show that the $q_{||}$ fall-off length steepens in the near-SOL reaching a minimum of 6-10 mm near the LCFS consistent with descriptions of the narrow feature. While the outboard side narrow feature is significantly wider than that observed on the inboard side (where $\lambda^{near}_{q|| \text{ RCP}}$ ~2mm), the fraction of the SOL power contained in the narrow feature match between the two sides. Furthermore, the power fractions scale together as a function of I_p and vanish together for $I_p \leq 90$ kA, suggesting that we are measuring the same phenomenon.

The strong poloidal asymmetry in $q^{near}_{||0}$ and $\lambda^{near}_{q||}$ observed in these experiments appears to explain why the narrow feature was rarely observed in measurements

from the outboard side, top, or bottom of the plasma. Poloidal asymmetries in the heat flux profiles have also been seen in GBS simulations, where the narrow feature exists within the T_e and n_e channels. Further study in these poloidal asymmetries is needed in order to predict the narrow feature heat flux profiles at the inner wall target.

Halpern [36] predicts that the narrow feature decay length should be related to the radial correlation length of the turbulence just outside the LCFS. This prediction is found to hold true for the outboard side where the radial correlation length was measured within the uncertainty of the measurements, even for conditions where the narrow feature is difficult to discern from the far SOL. This supports the hypothesis that radially sheared **E**x**B** poloidal flows outside the LCFS are responsible for the narrow feature.

Since the sheath currents to the target and the non-zero V_f profiles are believed to be related [25,26,36], a simple model of the floating potential profiles was proposed and tested. This model proposes that the non-zero V_f profiles arise from the circulation of parallel currents within the SOL driven by divergences in the polarization and diamagnetic cross-field currents. The model correctly reproduces the general shape of the V_f profiles, and the predicted values for $V_{f,\min}$ at the LCFS were found to match with the measurements for all values of I_p.

In conclusion, the narrow feature does exist on the outboard side, and although it is wider and weaker, it has been shown to be consistent with the measurements of the narrow feature on the inboard side. We have shown that the measurements are consistent with analytical models predicting that polarization and diamagnetic cross-field currents drive **E**x**B** shear flows which limit cross-field turbulent transport, causing the narrow feature.

5. Acknowledgements

This work was supported by the U.S. Department of Energy under Grant No. DE-SC0010529, and Award No. DE-FG02-95ER54309, and was carried out within the framework of the EUROfusion Consortium and has received funding from the

Euratom research and training programme 2014-2018 under grant agreement No 633053. The views and opinions expressed herein do not necessarily reflect those of the European Commission. The technical contributions of L. Chousal and R. Hernandez are gratefully acknowledged. We also thank R. Pitts for his leadership in this field.

6. Figures

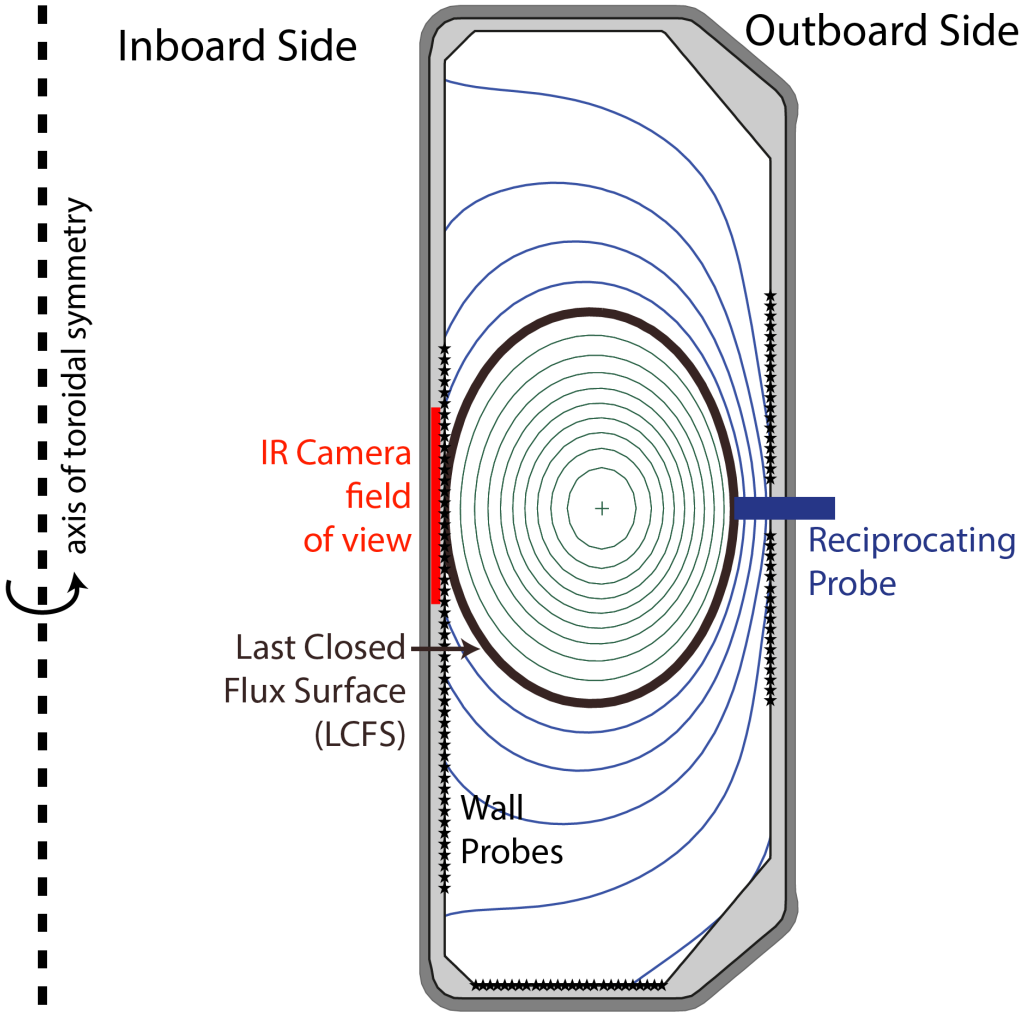

Figure 1 Plasma equilibrium for an elliptical plasma limited on the central column of the TCV tokamak with the locations of the Reciprocating probe (in blue), the IR camera field of view (in red), and the wall Langmuir probes (black stars). The contour of the first wall tiles is shown in light grey within the dark grey boundary which signifies the vacuum vessel.

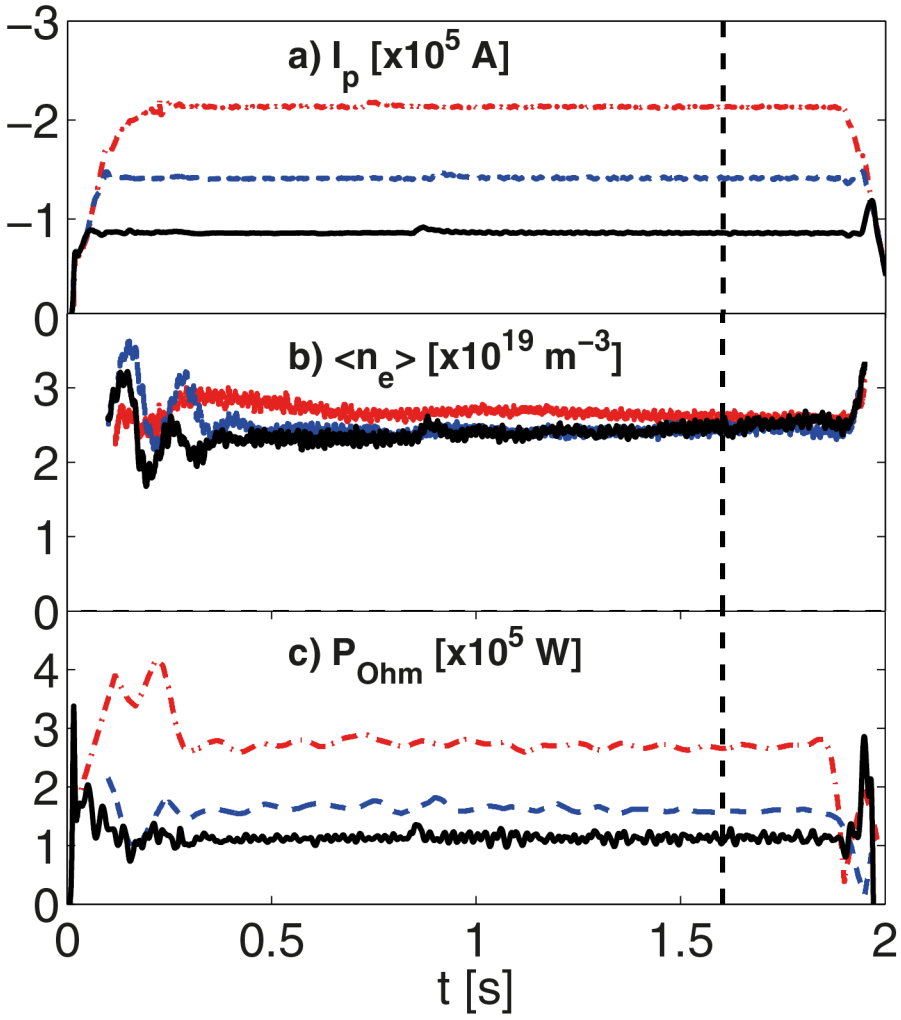

Figure 2 I_p was scanned for each discharge with 3 examples shown above (a) with I_p = 85, 140, and 210 kA shown in the black line, dashed blue line, and dot-dashed red lines respectively. The line-average density (b) was held constant across the scan, and is stable from 0.4s through to the end of each discharge. The input ohmic power (c) varies with plasma current, and is also well controlled. The reciprocating probe took data at 1.6s as shown by the vertical dashed line.

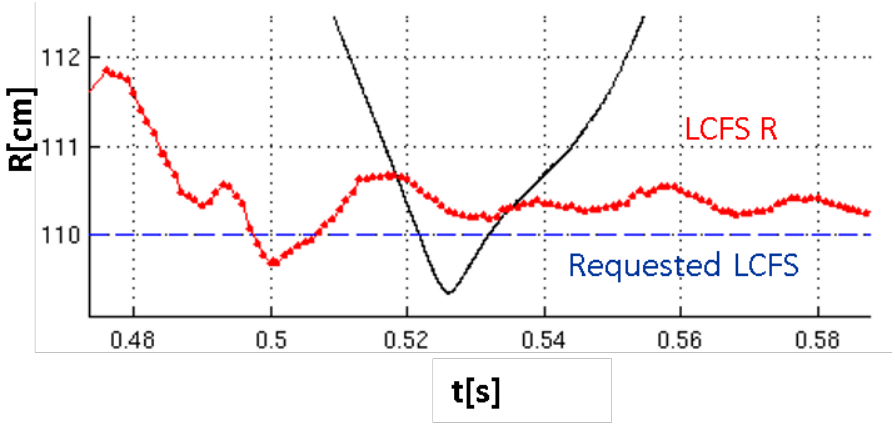

Figure 3 The outboard LCFS radius (dotted line) and RCP electrode radius (solid line) at z=0 as a function of time. The LCFS of the plasma changes significantly throughout the probe plunge. Thus, the normalized coordinates are calculated using equilibrium reconstructions generated with a 1 ms resolution.

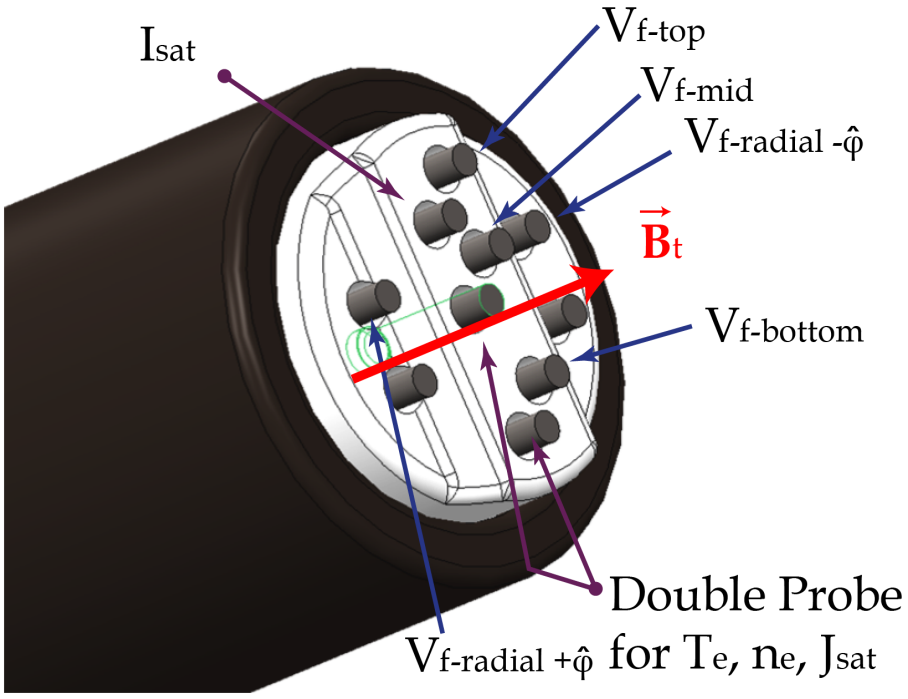

Figure 4 The probe head from the Fast Reciprocating Probe at TCV shows the electrode arrangement. The relevant diagnostics for this study are labeled. The electrodes are 1.5mm in diameter and extend 1.5 mm beyond the boron nitride insulator (white). The carbon shroud is 2.5 cm in diameter. The radially recessed tips only receive plasma flux along the magnetic field in one direction, and are set back by 1.57 mm.

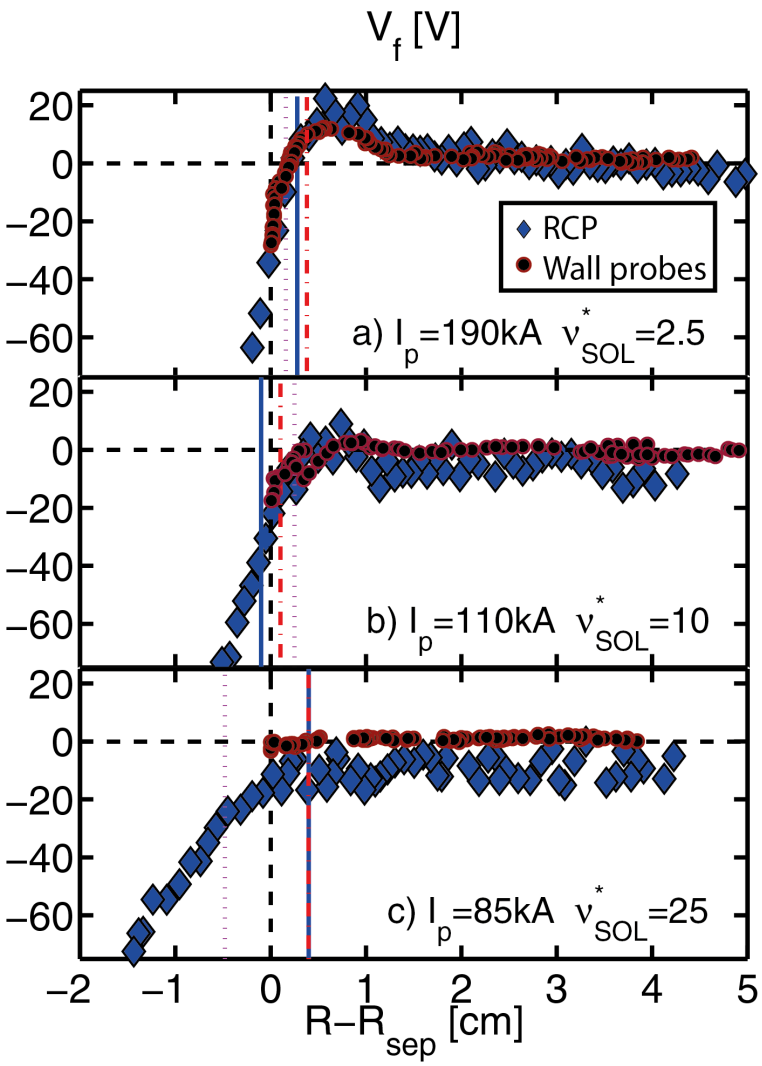

Figure 5 The V_f measurements from the RCP (diamonds) and from central column mounted probes (circles) from discharges with a) I_p = 190 kA, and ν^*_{SOL} = 2.5, b) I_p = 110 kA, and ν^*_{SOL} = 10, and c) I_p = 85 kA, and ν^*_{SOL} = 25. A steep drop in V_f from both the RCP and wall probes is seen within the SOL as well as a positive excursion spanning from 2-10mm into the SOL is seen in (a and b). V_f profiles align very well between the wall probes and the RCP, indicating that V_f is constant along field lines. The RCP profiles have been shifted to match the wall probes placing the LCFS at the black dashed line at $R-R_{sep}$ =0. For comparison, the LCFS position is shown as defined by LIUQE (dark blue line), the velocity shear layer (red dot-dashed line), and the minimum in $\partial^2 V_f / \partial R^2$ (purple dotted line).

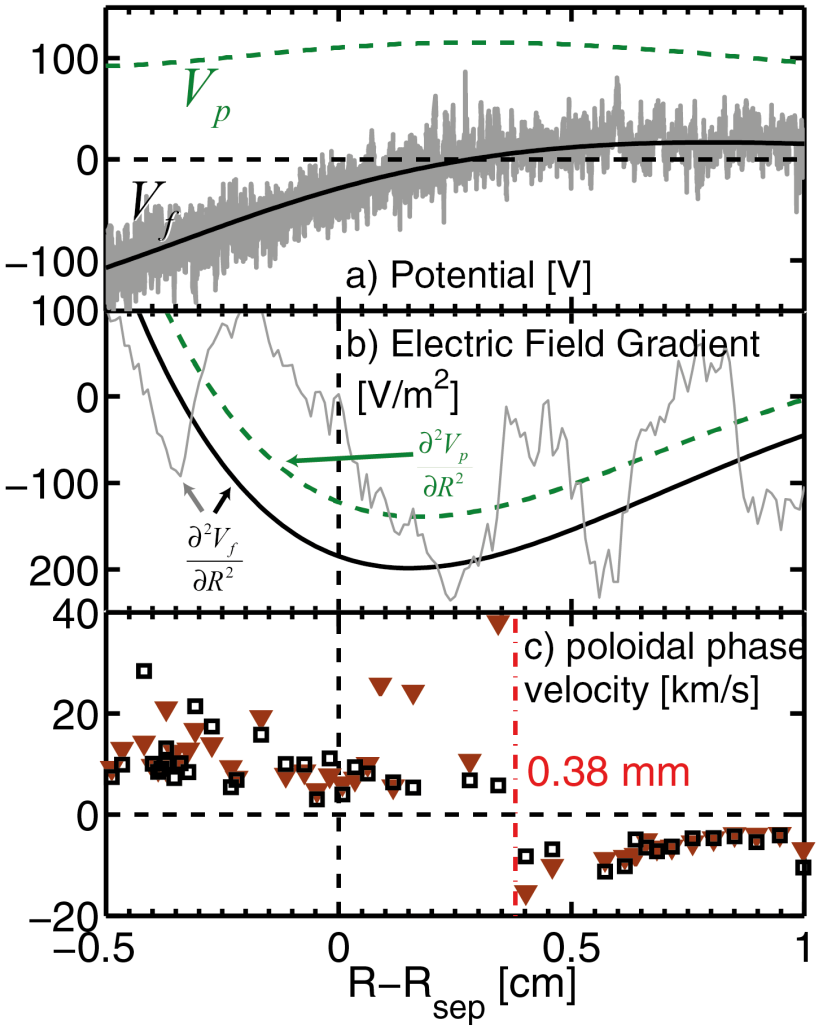

Figure 6 Alternative prescriptions for identifying the location of the LCFS for the I_p = 190 kA, ν^*_{SOL} =2.5 case using (a,b) the maximum rate of change in E_r. The lines plotted show polynomial fits to the voltage (a) and the second derivative of those fits (b) of V_f (solid) and V_p (dashed). The grey region in (a) shows the the scatter in V_f, and the grey line in (b) is $\partial^2 V_f / \partial R^2$ as fit by local 2nd order polynomials, and is intended to represent the scatter in the $\partial^2 V_f / \partial R^2$ fit. V_p was calculated using $V_p = V_f + 2.5kT_e$ with polynomial fits to V_f and T_e. Due to the significant intermittency in the T_e profiles, the scatter for V_p is not shown as it would be off-scale. Since any fit to T_e tends to smooth the second derivatives, there is no clear difference between the minima in $\partial^2 V_p / \partial R^2$ and $\partial^2 V_f / \partial R^2$, which we estimate to be 1.5 mm outside the LCFS. The velocity shear layer (c) is defined where the poloidal phase velocity changes sign, as determined using poloidal cross-correlation. In this example, it occurs 3.8 mm outside the LCFS which corresponds roughly with the maximum in V_p.

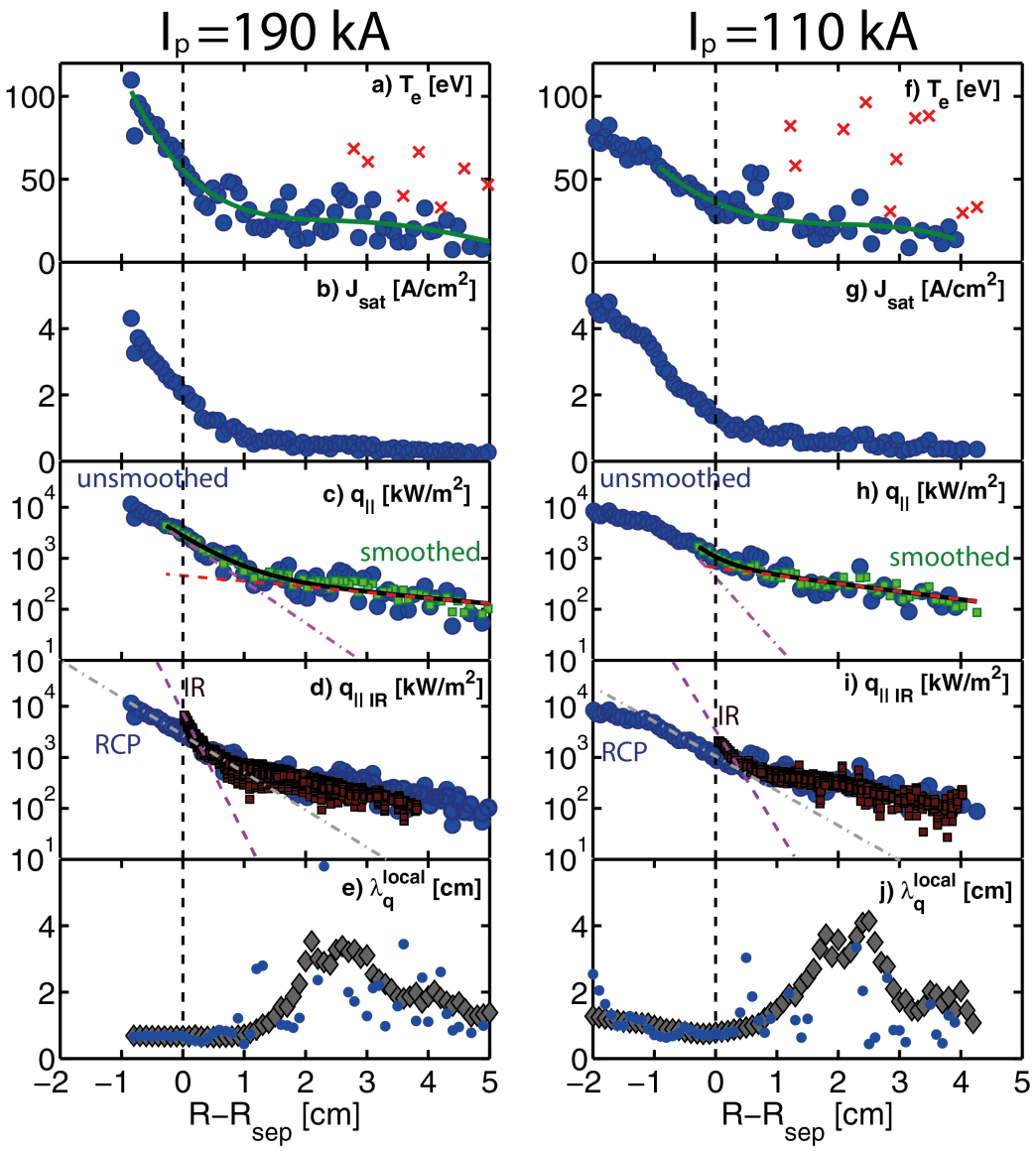

Figure 7 probe data from Ip = 190 kA (left column) and Ip = 110 kA (right column). Te from double-probe IV fits (a,f) where the red 'x's are data rejected based on their goodness of fit. The green line is a polynomial fit to the data. Jsat from double-probe IV fits (b,g). $q_{||}$ (c,h) are calculated from double probe fits (blue circles) and from the T_e trendline (green squares). The trendline (black) is a sum of exponentials where the exponential components represent the far SOL (red dashed line) and near SOL (purple dotted dashed line). The RCP $q_{||}$ is plotted again against the IR camera data from the central column (red squares) in (d,i). Dashed lines draw the eye to the steep regions near the LCFS. The local decay length (e,j) determined from single exponentials fitted to 2cm (diamonds) or 5mm (circles) data windows of the RCP $q_{||}$ profiles.

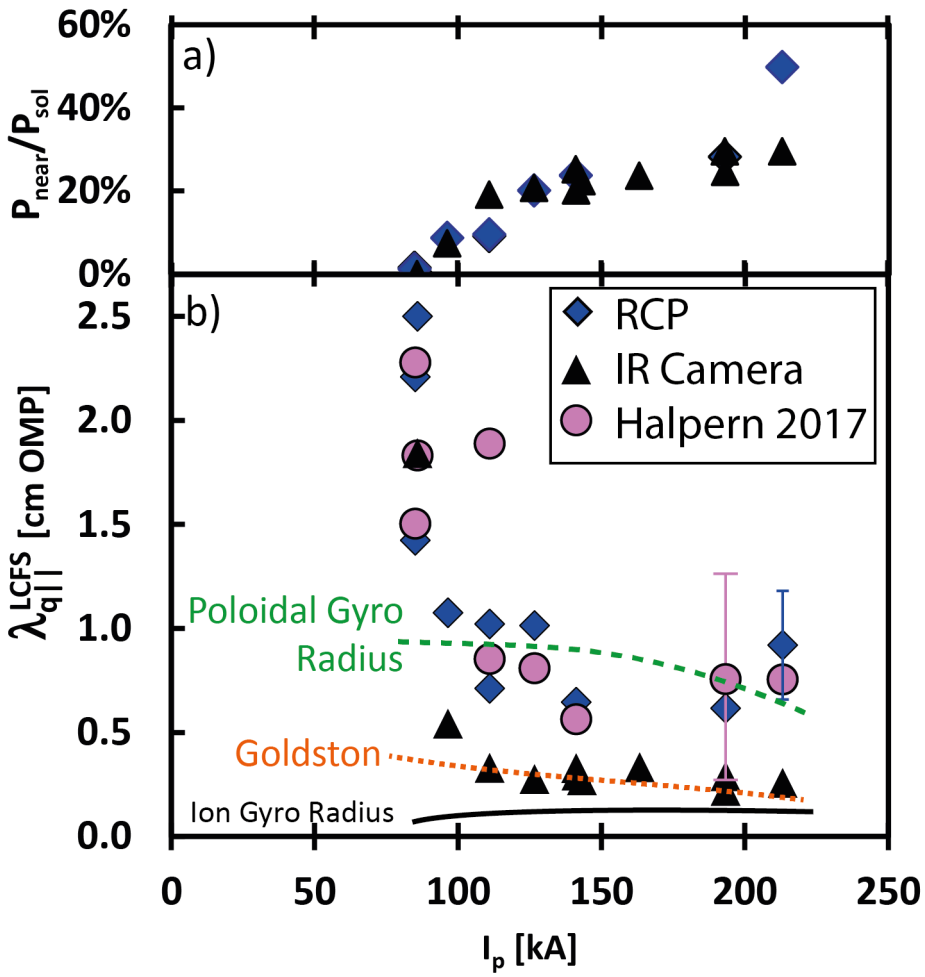

Figure 8 a) The narrow feature power fraction for the RCP (blue diamonds) and the IR camera (red triangles).

b) The heatflux decay lengths at the LCFS from the RCP (blue diamonds) and by the IR camera (black triangles). The error bars show the 2σ uncertainty typical for their respective datasets; for the IR measurements, the error bars are smaller than the datapoints. The ion gyro radius (black line) and poloidal gyro radius (green dashed line) are calculated on the LFS assuming $T_i = 3T_e$. The Goldston Heuristic-Drift scaling (gold dotted line) is calculated as in [44]. The Halpern Scaling [36] is calculated by from the radial cross-correlation length from two V_f pins (circles).

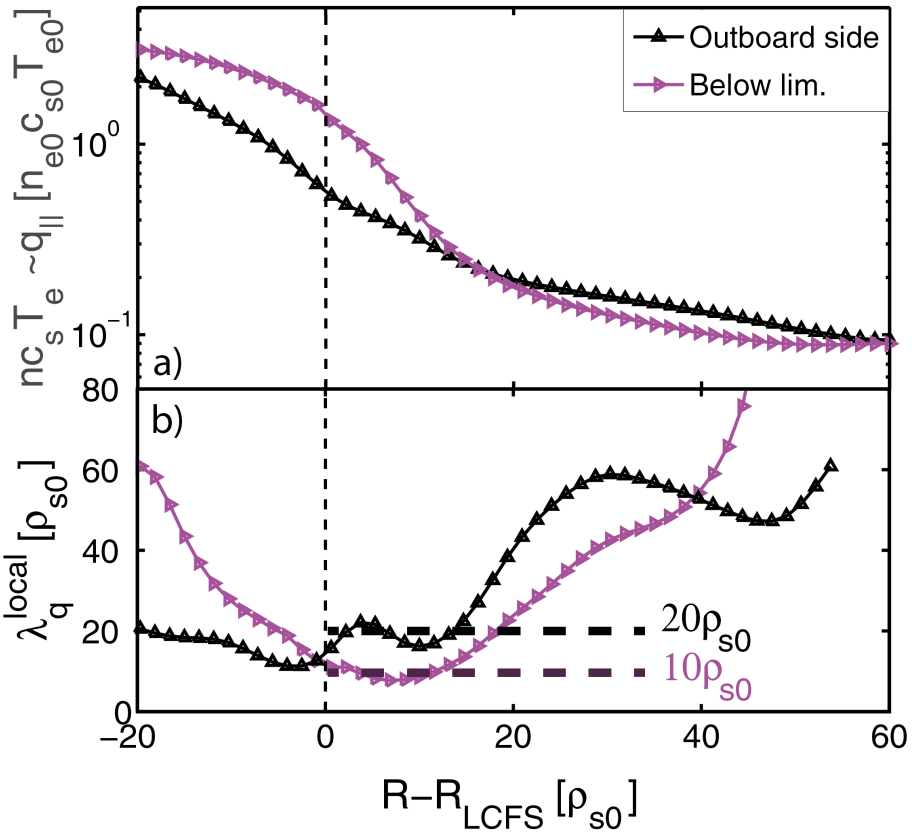

Figure 9 Poloidal asymmetries in the narrow feature from a GBS simulation. The $q_{||}$ profiles (a) for the inboard side just below the limiter and for the outboard side from the simulations described in [36] reproduced from Figure 1 therein. The local fall-off lengths (b) for the two profiles in (a) as a function of radius. The narrow feature width varies by a factor of 2.

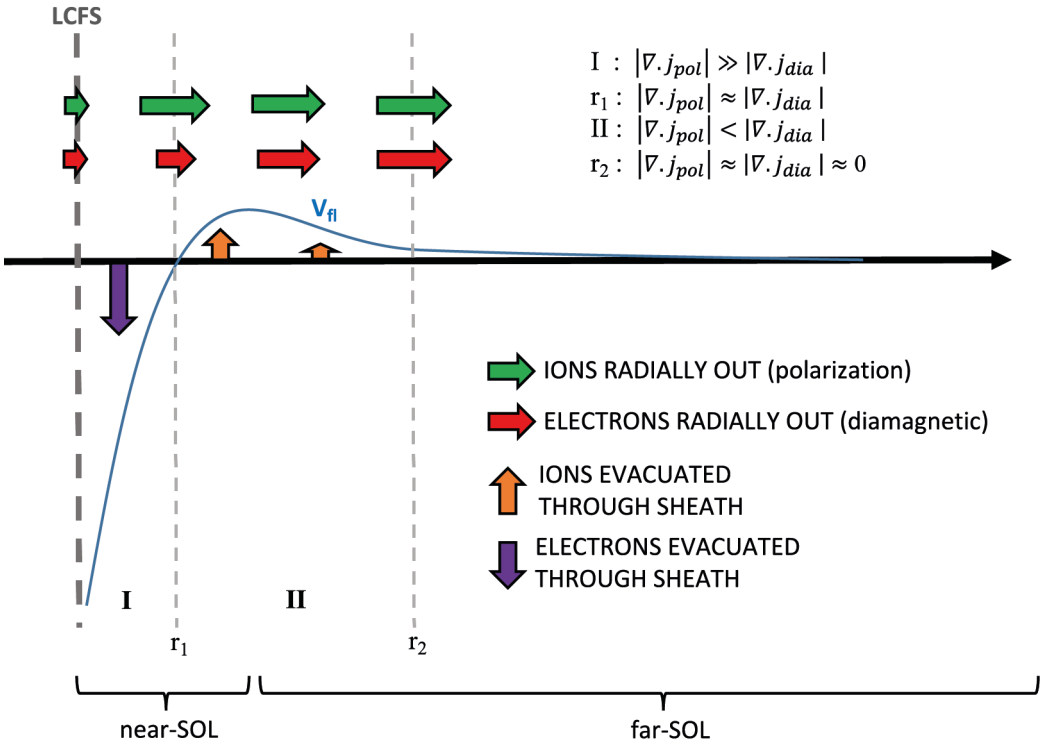

Figure 10 A schematic of the SOL current model. The floating potential profile structure is related to parallel sheath currents created by the interplay of radial polarization and diamagnetic currents. We indicate the various regions where the divergences of the currents lead to net electron (I) or net ion (II) currents through the sheath.

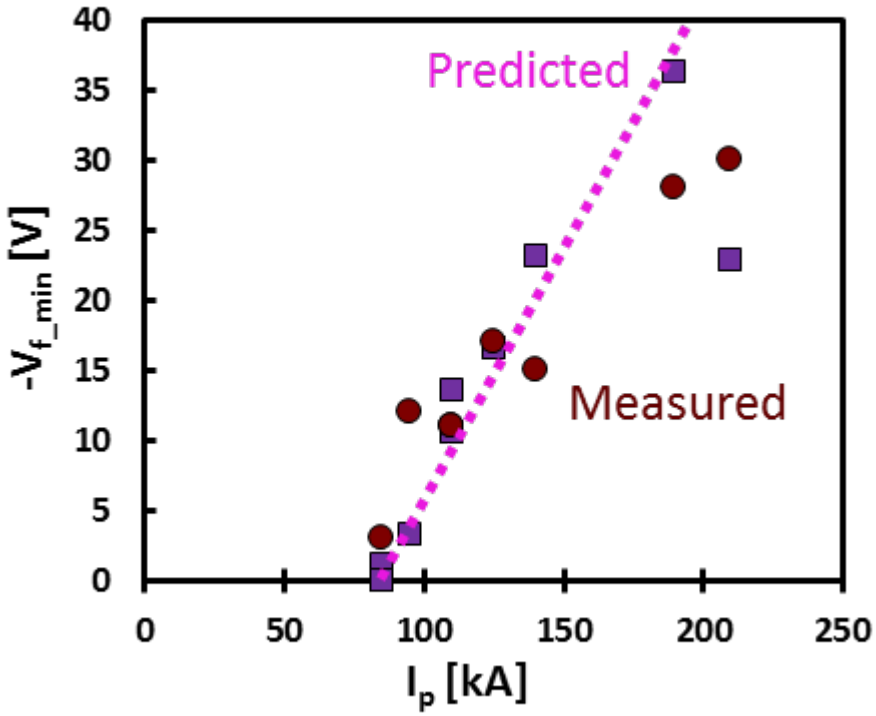

Figure 11 The magnitude of the drop in floating potential as measured by the target Langmuir probes (red circles) and those calculated (purple squares) using Eqn 12 as a function of T_e, λ_p, ρ_s, and q taken from RCP profiles and the magnetic reconstruction.

7. References

[1] Pitts R A, Carpentier S and Escourbiac F 2011 *J. Nucl. Mater.* **415** S957–64
[2] Casper T, Gribov Y, Kavin a., et al 2014 *Nucl. Fusion* **54** 13005
[3] Loarte A, Lipschultz B, Kukushkin a. . S, et al 2007 *Nucl. Fusion* **47** S203–63
[4] Horacek J, Pitts R A, Adamek J, et al 2016 *Plasma Phys. Control. Fusion* **58** 74005
[5] Rudakov D L, Boedo J a., Pitts R a., et al 2011 *J. Nucl. Mater.* **415** S387–90
[6] Kočan M, Gunn J P, Kocan M and Gunn J P 2010 *Plasma Phys. Control. Fusion* **52** 45010
[7] Silva C, Arnoux G, Devaux S, et al 2014 *Nucl. Fusion* **54** 83022
[8] Chankin A V, Chicherov V M, Efstigneev S A, et al 1987 *J. Nucl. Mater.* **145–147** 789–92
[9] Stangeby P C, Pitcher C S and Elder J D 1992 *Nucl. Fusion* **32** 2079–89
[10] Denner T, Finken K ., Mank G and Noda N 1999 *Nucl. Fusion* **39** 83–94
[11] Finken K H, Denner T and Mank G 2000 *Nucl. Fusion* **40** 339–55
[12] Arnoux G, Farley T, Silva C, et al 2013 *Nucl. Fusion* **53** 73016
[13] Horacek J, Vondracek P, Panek R, et al 2014 *J. Nucl. Mater.* **463** 385–8
[14] Nespoli F, Labit B, Furno I, Canal G P and Fasoli A 2015 *J. Nucl. Mater.* **463** 393–6
[15] Marmar E S, Baek S G, Barnard H, et al 2015 *Nucl. Fusion* **55** 104020
[16] Tsui C K, Taussig D A, Watkins M G, Boivin R L and Stangeby P C 2012 *Rev. Sci. Instrum.* **83**10D723
[17] Stangeby P C, Tsui C K, Lasnier C J, et al 2014 *J. Nucl. Mater.* **463** 0–3
[18] Kocan M, Pitts R A, Arnoux G, et al 2015 *Nucl. Fusion* **55**
[19] Sergienko G, Arnoux G, Devaux S, et al 2014 *Phys. Scr.* **T159** 1–5
[20] Arnoux G, Balboa I, Clever M, et al 2014 *Phys. Scr.* **2014** 14009
[21] Matthews G F, Bazylev B, Baron-Wiechec A, et al 2016 *Phys. Scr.* **2016** 14070
[22] Labombard B, Kuang A, Brunner D, et al 2016 **0** 1–9
[23] Bak J G, Pitts R A, Kim H S, et al 2016 *Nucl. Mater. Energy* **0** 1–7
[24] Pitts R A, Chavan R and Moret J-M 1999 *Nucl. Fusion* **39** 1433
[25] Nespoli F, Labit B, Furno I, et al 2017 *Submitted to Nucl. Fusion*
[26] Labit B, Nespoli F, Horacek J, et al 2016 *Proc. of the 26th IAEA Fusion Energy Conference* (Kyoto)
[27] Pitts R A, Alberti S, Blanchard P, et al 2003 *Nucl. Fusion* **43** 1145–66
[28] Boedo J A, Crocker N, Chousal L, et al 2009 *Rev. Sci. Instrum.* **80** 123506
[29] Tsui C K, Boedo J A and Stangeby P *in preparation*
[30] Moret J-M, Duval B P, Le H B, et al 2015 *Fusion Eng. Des.* **91** 1–15
[31] Stangeby P C C, Canik J M M, Elder D, et al 2015 *Nucl. Fusion* **55** 93014
[32] Makowski M A, Lasnier C J, Leonard A W, et al 2013 *J. Nucl. Mater.* **438** S208–11
[33] Sheikh U A, Duval B P, Labit B and Nespoli F 2016 *Rev. Sci. Instrum.* **87** 1–4
[34] Groebner R J, Burrell K H and Seraydarian R P 1990 *Phys. Rev. Lett.* **64** 3015–8
[35] Stangeby P C 2000 *The Plasma Boundary of Magnetic Fusion Devices* (Taylor & Francis Group)
[36] Halpern F D and Ricci P 2017 *Nucl. Fusion* **57** 34001
[37] Suzuki Y, Ida K, Kamiya K, et al 2013 *Nucl. Fusion* **53** 2–7

[38] Brotankova J, Stockel J, Horacek J, et al 2009 *Plasma Phys. Reports* **35** 980–6
[39] Boedo J A *Pers. Commun.*
[40] McKee G R, Petty C C, Waltz R E, et al 2002 *Nucl. Fusion* **41** 1235–42
[41] Lister J B, Hofmann F, Moret J-M, et al 1997 *Fusion Sci. Technol.* **32** 321–73
[42] Marki J, Pitts R a., Eich T, et al 2007 *J. Nucl. Mater.* **363–365** 382–8
[43] Kočan M, Gunn J P, Pascal J-Y, et al 2008 *Plasma Phys. Control. Fusion* **50** 125009
[44] Goldston R J 2015 *J. Nucl. Mater.* **463** 397–400
[45] Goldston R J 2012 *Nucl. Fusion* **52** 13009
[46] Ricci P, Halpern F D, Jolliet S, et al 2012 *Plasma Phys. Control. Fusion* **54** 124047
[47] Nespoli F, Furno I, Halpern F D, et al 2016 *Nucl. Mater. Energy* **0** 1–4
[48] Loizu J, Ricci P, Halpern F D, Jolliet S and Mosetto A 2014 *Nucl. Fusion* **54** 83033
[49] Nespoli F, Avino F, Furno I, et al 2017 *Under Peer Review*
[50] Dejarnac R, Stangeby P C, Goldston R J, et al 2015 *J. Nucl. Mater.* **463** 381–4
[51] Loizu J et al *in preparation*
[52] Ricci P and Rogers B N 2013 *Phys. Plasmas* **20** 1–4